Journal of Aerospace Information Systems,
Volume 19, Number 7, July 2022, pp. 504-510
DOI:10.2514/1.I011035

Rapid Method for Computing Reachable Landing Distances in Helicopter Autorotative Descent

Brian F. Eberle *, and Jonathan D. Rogers†
Georgia Institute of Technology, Atlanta, GA, 30332

Mushfiqul Alam ‡, and Michael Jump§
University of Liverpool, Liverpool, UK, L69 3GH

I. Introduction

Rapid selection of a suitable landing site is critical to the success of helicopter autorotation following power loss or transmission failure. Numerous factors may influence a pilot's ability to select a suitable landing location including workload, visibility, and uncertainty regarding aircraft glide performance. Given the numerous tasks pilots must perform in emergency scenarios (troubleshooting, communication, maintaining stable flight, and establishing a safe descent), there is significant potential utility for pilot aids that enhance the pilot's ability to rapidly evaluate and select one or more potential landing sites. The faster a landing site can be selected, the more time the pilot has to configure the aircraft to reach the selected location and plan any necessary maneuvers to execute a successful descent. Pilot aides that enhance landing site selection capability may be implemented using head-up or head-down displays. A relatively simple cue that may be useful to pilots involves the projection of the area on the ground that is reachable by the aircraft. If such a "reachable footprint" can be effectively displayed, it may allow the pilot to quickly determine which possible landing points are within the glide capability of the aircraft, thereby eliminating any need to estimate glide distance over the ground and reducing the impact of uncertainty in glide range.

There has been considerable research in the area of autorotation pilot cueing and automated control over the past decade. Throughout this research, there is a recurring differentiation between the two primary phases of the autorotation maneuver. The first phase is the steady-state descent phase and is characterized by the establishment of an energy trade between potential energy and kinetic energy of the vehicle and rotor. The second phase is the flare, in which the aircraft uses the stored rotor energy to reduce its vertical and horizontal speed. Numerous authors have proposed the use of visual [1–6] or haptic cues [7–9] to enhance pilot control performance in both of these phases. In addition, several types of control algorithms have been developed to fully automate various portions of the autorotation maneuver [10–13]. Two interesting examples of fully-automated autorotation control are those by Grande and Langelaan [12], which developed an optimal control law for the flare phase, and the path planning method developed by Yomchinda *et al.* [14] which

*Graduate Research Assistant, Mechanical Engineering, Atlanta, GA 30313
†Lockheed Martin Associate Professor, Aerospace Engineering, 270 Ferst Dr, Atlanta, GA 30313, AIAA Associate Fellow.
‡Post-doctoral Research Associate, Dept. of Mechanical, Materials and Aerospace Engineering, Liverpool, UK L69 3GH
§Senior Lecturer, Dept. of Mechanical, Materials and Aerospace Engineering, Liverpool, UK L69 3GH, Member AIAA

Published by AIAA. This is the Author Accepted Manuscript issued with: Creative Commons Attribution Non-Commercial License (CC:BY:NC 4.0).
The final published version (version of record) is available online at DOI:10.2514/1.I011035.. Please refer to any applicable publisher terms of use.

generates a feasible Dubins trajectory from the current vehicle location to the selected landing point. Nevertheless, despite the extensive research performed in the area of autorotation control augmentation, there has been little to no research to date on methdologies for improving landing site selection during autorotation. Interestingly, automated reachability analysis and pilot cueing for engine-out scenarios in fixed-wing aircraft has been studied extensively [15–21] and has been shown to reduce pilot workload [17]. This work is not directly translatable to rotorcraft because the lift-to-drag ratio of helicopters in autorotation is typically much less than for fixed-wing aircraft, leading to shorter glide distances from a given altitude and speed. Furthermore, the descent rate variation with respect to bank angle during autorotation is highly nonlinear (as will be subsequently shown), meaning that specialized analysis must be performed to capture the altitude loss during turning autorotative flight within the reachability algorithm. Finally, the helicopter's attainable trim condition in descent depends on its speed and altitude when the autorotation is initiated – if the failure occurs at low speed and low altitude, the reachability analysis must be performed assuming a very low forward speed. As a result, dedicated reachability determination algorithms must be developed for helicopters that can account for low lift-to-drag ratios, autorotation-specific turning performance, and the wide range of glide conditions that may be necessary depending on the maneuver's initial condition.

This engineering note describes a reachability determination algorithm for helicopters that is designed to rapidly compute the reachable landing locations on the ground, termed the "reachable footprint", when autorotating from the current aircraft location. For a given desired heading, the algorithm assumes that the aircraft turns to the desired immediately and flies a straight-line descent thereafter. A kinematic model is used to predict how far the aircraft can reach when flying this heading. This process is repeated for all possible headings, leading to a reachable footprint in any direction. The algorithm accounts for winds, descent rate differences in turns and forward flight, and variable trim conditions in the steady-state descent. The footprint can then be displayed to the pilot to quickly evaluate whether candidate landing sites are inside or outside the footprint. Note that in the current work, the term "reachability" is used informally and is not invoked in the rigorous control-theoretic sense, as in [12].

The note proceeds as follows. First, the reachability algorithm is presented in detail. Example simulation results are presented for the UH-60 helicopter, illustrating the evolution of the reachable footprint as the aircraft descends as well as the effects of winds. An additional simulation example shows how the algorithm can be used in non-flat terrain through the incorporation of ray tracing. A limited set of flight trials is also described in which the algorithm is used to drive markers on a head-up display pilots use the cue to select a landing site for autorotation. The final section presents conclusions of the work and suggestions for future research.

II. Reachability Calculation Algorithm

The goal of the reachability calculation algorithm is to evaluate the furthest points to which the aircraft can glide from its current state, including the effects of wind and terrain. These points can be calculated in a 360 deg circle

around the aircraft, leading to the notion of a "reachable footprint". For a given aircraft state, the extent and shape of the reachable footprint will be dependent on numerous factors including the aircraft glide performance at its current gross weight, winds, terrain, and pilot skill. The footprint calculation algorithm proposed here accounts for as many of these factors as possible while still retaining a simple, model-free form conducive to rapid calculation. Note that the purpose of the footprint is to provide the pilot with a visualization of the maximum possible glide area. In a fully-implemented system, it may be necessary to account the flare maneuver and/or a final turn into the wind near the end of the autorotation by slightly reducing the estimated glide distance, although such considerations are not explored here. Likewise, it may be advantageous to couple the footprint generation scheme with a path planner such as that proposed by [14] to plan a trajectory to the selected landing point in the interior of the footprint. Such extensions are not explored here but are worthy of further investigation.

Consider a standard North-East-Down (NED) inertial reference frame depicted in Fig. 1 with unit vectors $\vec{I}_I$, $\vec{J}_I$, and $\vec{K}_I$. The position vector of the aircraft mass center (point C) is given by $\vec{r}_{O\to C} = x\vec{I}_I + y\vec{J}_I + z\vec{K}_I$, where point O is the origin of the inertial frame. A wind frame W is also defined that is aligned with the NED frame but moves with the assumed constant wind. Let the wind vector be defined as $\vec{v}_{W/I} = W_m \cos(\psi_w)\vec{I}_I + W_m \sin(\psi_w)\vec{J}_I$. At the instant of planning, the aircraft is located at (x_0, y_0, z_0) with velocity with respect to the wind frame given by $\vec{v}_{B/W} = u\cos(\psi_0)\vec{I}_W + u\sin(\psi_0)\vec{J}_W$. Given a selected final heading ψ_f, a two-stage path is planned consisting of an initial turn from ψ_f to ψ_0 with a constant heading rate $\dot{\psi}$, followed by a straight line path until intersection with the ground plane. It is assumed that the aircraft descends at a constant rate in the turn ($\dot{z}_t$), and a different constant rate during the straight segment ($\dot{z}_s$). It is also assumed that the aircraft has an estimate of the current wind speed and direction.

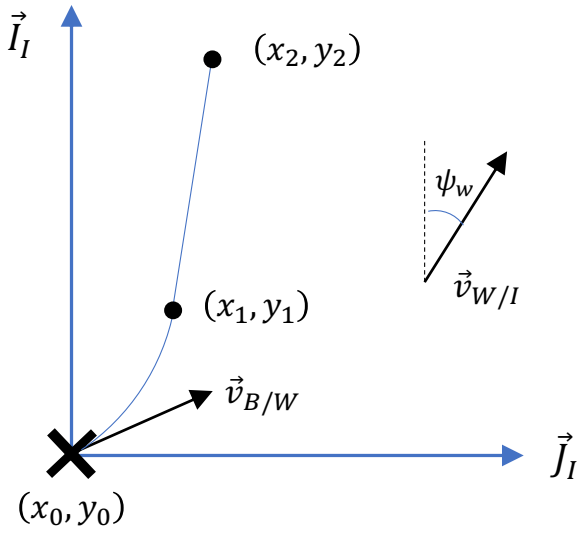


Fig. 1 Turn and Straight Segment Planning Diagram.

If the terrain is flat, the location at which the vehicle intersects the ground plane (x_2, y_2) can be easily calculated using standard kinematics. First, the location at which the aircraft completes the turn, denoted as (x_1, y_1, z_1) in Fig. 1, is given by,

$$x_1 = W\cos\psi_w t_1 + \frac{u}{\psi_f - \psi_0}(\sin\psi_f - \sin\psi_0)t_1 + x_0 \tag{1}$$

$$y_1 = W\sin\psi_w t_1 + \frac{u}{\psi_f - \psi_0}(\cos\psi_0 - \cos\psi_f)t_1 + y_0 \tag{2}$$

$$z_1 = z_0 + \dot{z}_t t_1 \tag{3}$$

where $t_1 = (\psi_f - \psi_0)/\dot{\psi}$ is the time needed to complete the constant-rate turn (note that, in the implementation described here, additional logic is included to determine whether the aircraft should turn right or left to change heading from ψ_0 to ψ_f in order to minimize t_1). After the turn is completed, the final heading is maintained until the aircraft reaches the ground plane ($z = 0$). The final position is then,

$$x_2 = x_1 + (t_2 - t_1)(u\cos\psi_f + W\cos\psi_w) \tag{4}$$

$$y_2 = y_1 + (t_2 - t_1)(u\sin\psi_f + W\sin\psi_w) \tag{5}$$

where

$$t_2 = \frac{z_1}{\dot{z}_s} + t_1 \tag{6}$$

To complete the footprint, impact locations (x_2, y_2) are computed for an array of candidate ψ_f values, evenly spaced from 0 to 360 deg. Figure 2 shows the general shape of a footprint for an aircraft heading directly north with no wind. Several of the turn and straight line segments are shown for a few ψ_f values, with the points (x_1, y_1) and (x_2, y_2) labeled for an example path. Note that the distance the aircraft can glide from its current position decreases as the turn time t_1 becomes longer – this is because the descent rate in a turn in higher than that in straight flight ($\dot{z}_t > \dot{z}_s$). In the extreme case that the aircraft turns 180 deg around, the total glide distance is quite short at this example initial altitude compared to the straight-ahead glide distance. Overall, the shape of the reachable footprint changes noticeably as a function of initial altitude and winds, as will be shown in Section III.

In cases where the terrain is fairly flat, Eqs. (1)-(5) can be rapidly computed (for example, a Matlab implementation on a 2.6 GHz processor yielded an average computation time of 7.2 μs). Thus, the footprint can be rapidly recomputed as the aircraft descends and provided to a head-up or head-down display for pilot cueing. If the terrain is not flat, the shape of the reachable footprint can change significantly. If digital terrain data is available, rapid ray tracing schemes [22, 23] may be used to compute the intersection of the paths for each ψ_f with the terrain. The parallel nature of many

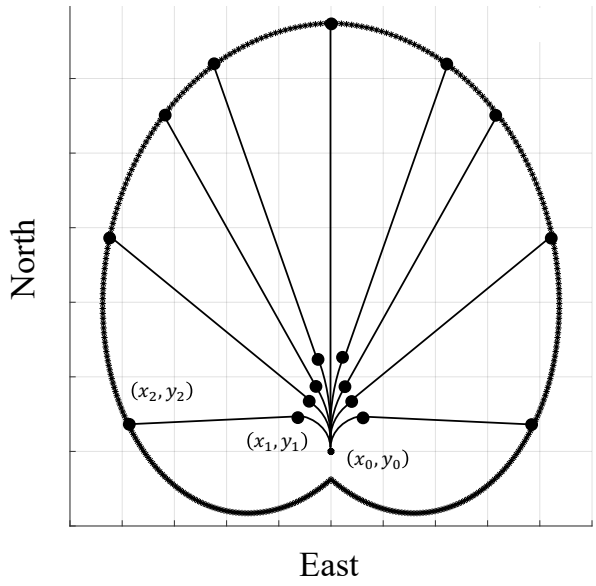


Fig. 2 Example Reachable Footprint with Various Paths.

advanced ray tracing methods means that such an implementation may benefit from emerging embedded graphics processing units, which are increasingly being incorporated into autonomous vehicles. An example ray tracing solution for the reachable footprint in non-flat terrain is provided in Section III.

III. Simulation Results

A series of simulation studies are shown in this section to examine the effects of various parameters of the algorithm and to explore how the shape of the reachable footprints change as a function of wind, vehicle height, and non-flat terrain. The example aircraft model used throughout this section is the UH-60. In the following subsection, where algorithm parameters are derived through simulation, a 6-degree-of-freedom (6DOF) nonlinear flight dynamic model of the UH-60 is employed. A detailed description of this model is provided in [11, 24] but is omitted here for brevity.

A. Descent Rate Study

The algorithm described in Section II requires several parameters: the vehicle airspeed in autorotation (u), turn rate in autorotation ($\dot{\psi}$), and descent rates in level flight ($\dot{z}_s$) and turning flight ($\dot{z}_t$). In the steady-state autorotative descent, various autorotative trim conditions exist for airspeed, descent rate, and rotor speed, and selection of the desired trim condition in descent is based on pilot objectives for maximizing glide distance or maximizing time aloft. Thus, the algorithm implemented in this work uses the current airspeed of the aircraft to generate the footprint, thereby adapting the footprint to the pilot's selected airspeed in autorotative descent. However, the turn rate and descent parameters ($\dot{\psi}$, $\dot{z}_s$, $\dot{z}_t$) must be selected in order to calculate the footprint at the current airspeed. When selecting these parameters,

the coupling between the turn rate $\dot{\psi}$ and the descent rate in the turn, $\dot{z}_t$, must be accurately captured. Furthermore, when turning to a particular heading, the pilot may turn at various possible turn rates (and resulting descent rates). The altitude loss that results in the turn affects the total glide distance. Since the turn rate that the pilot will select is unknown *a priori*, the algorithm should use a turn rate that leads to the shortest overall glide distance in order to maintain a conservative prediction of the footprint. Note that the notion of "conservative" in this case refers to the desire to underpredict the glide range rather than overpredict it, given the uncertainty in the turn profile that the pilot will select. In this section, a 6DOF simulation of the UH-60 is used to determine algorithm parameters $\dot{\psi}$, $\dot{z}_s$, and $\dot{z}_t$ that generate a conservative reachable footprint. Note that comparable studies have been performed for fixed-wing aircraft [15–17], but this type of analysis has not been performed in the context of helicopter autorotation to the authors' knowledge.

To obtain the set of parameters that produces the most conservative reachability estimate, the UH-60 model was trimmed in autorotation starting at an altitude of at three forward flight speeds: 60 kts, 80 kts, and 100 kts. Once the aircraft was trimmed, constant angle of bank turns were executed at various bank angles until a 180 deg heading change was complete. The aircraft then flew a straight-line path until a fixed simulation time, which was the same for all runs across the various bank angles. A cascaded PID control scheme described in [24] was used to fly the above autorotation flight segments. For each trial, the descent rate in the turn and the percentage increase in the turning descent rate compared to the level flight descent rate were recorded, as shown in Figs. 3(a) and 3(b). Furthermore, the altitude lost in the turn and the total altitude lost for the fixed simulation time were recorded for each case, as shown in Figs. 3(c) and 3(d).

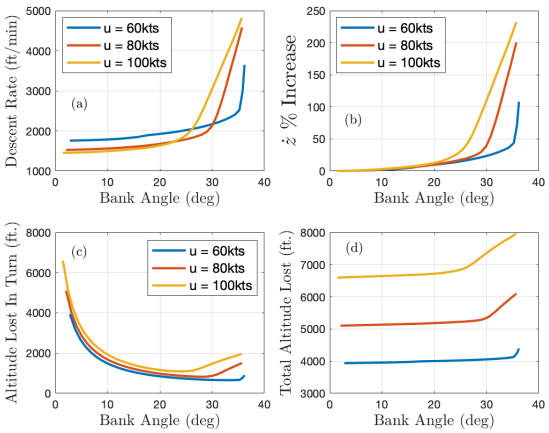


Fig. 3 Results of UH-60 Model Autorotative Descent Rate Study.

Several trends are evident in these figures. First, as expected, higher bank angles yield faster descent rates, although a significant increase in descent rate is observed beyond approximately 25 deg. Examining Fig. 3(c), however, shallower bank angles result in slower turn rates and thus longer times to complete the 180 deg. As a result, the total altitude lost in the turn is highest for the shallowest bank angles. However, for a given desired final heading (in this case, a

change in heading of 180 deg), it is not the amount of altitude lost in the turn that matters, but rather the total altitude lost during the turn and subsequent straight line segment. Figure 3(d) shows that, for any airspeed, the total altitude lost increases as the bank angle increases, with noticeable increases occurring beyond 25 deg. Thus, use of a larger bank angle will result in a more conservative footprint. For this work, a bank angle of 25 deg is assumed for the turn segments as this value represents a fairly aggressive turn without incurring the very steep descent rates that occur at higher bank angles. Selection of 25 deg angle of bank produces a balance between a footprint prediction that is useful and one that is overly conservative. For the 100 kts case (which produces the shortest glide), selection of 25 deg angle of bank yields $\dot{\psi}$ = 5.27 deg/s, $\dot{z}_s$ = 1464 ft/min, and $\dot{z}_t$ = 1890 ft/min.

To verify the conclusions of this study, reachable footprints were created for various bank angles assuming an initial altitude of 800 ft, airspeed of u = 100 kts, no winds, flat terrain, and initial heading of North. Figure 4 shows resulting footprints. At shallow bank angles (7 and 13 deg), the reachable footprint ends well in front of the aircraft because the vehicle cannot complete large heading changes before impact with the ground. It is clear that as the bank angle grows, the footprint becomes more smaller but also provides solutions closer to the aircraft since larger heading changes can be accomplished. However, at a bank angle of 31 deg, the descent rate increases drastically and the reachable footprint becomes extremely conservative. This provides evidence that the 25 deg angle of bank assumption produces a footprint that balances utility with conservativeness. It should be noted that turning performance in autorotation will vary depending on the aircraft, and thus this type of simulation study must be performed on an aircraft-specific basis to determine the specific conservative parameters to use for practical implementation.

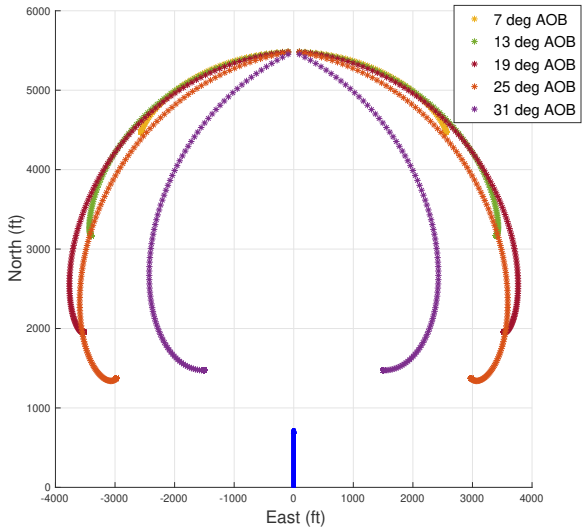


Fig. 4 Reachable Footprint at Varied Bank Angles.

B. Effects of Altitude and Wind

As the helicopter descends in autorotation, it is expected that the reachable footprint will continue to be updated and displayed to the pilot for situational awareness. It is interesting therefore to examine how the footprint evolves as the aircraft descends. To study this, reachable footprints were created at several altitudes assuming no winds and flat terrain using the following parameters: $u = 80$ kts, $\dot{z}_s = 1,525$ ft/min, $\dot{z}_t = 2,028$ ft/min, and $\dot{\psi} = 5.27$ deg/s. The footprints were created at different altitudes by progressing the (x_0, y_0) along the descent trajectory assuming no turn, simulating the aircraft flying a straight and level autorotative descent on a heading of North. Figure 5 shows how the footprints evolve as the aircraft descends (where the single dot at $x = 0$ for each color corresponds to the aircraft's (x_0, y_0) position at that altitude). At higher altitudes, the aircraft can complete turns to most final headings before reaching the ground. As the aircraft descends, the predicted reachable area becomes smaller, as expected, and the footprints are limited to a smaller range of heading changes.

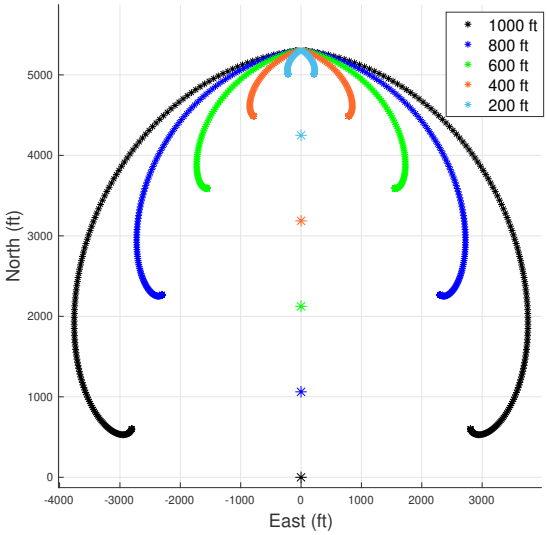


Fig. 5 Reachable Footprints as Varied Initial Altitudes.

Winds can substantially alter the shape of the predicted reachable footprint. To examine this, a footprint was calculated using the same parameters as above, except with a steady wind of $W = 6$ kts from the south-southwest direction ($\psi_w = 195$ deg), as depicted by the arrow in Fig. 6. The aircraft begins from $(x_0, y_0) = (0, 0)$, $z_0 = 1000$ ft, and $\psi_0 = 015$ deg. As expected, the footprint is skewed and extended in the downwind direction. It would be expected that, if implemented as part of an onboard avionics package, the footprint would evolve in real-time as estimated winds changed to aid pilot decision-making.

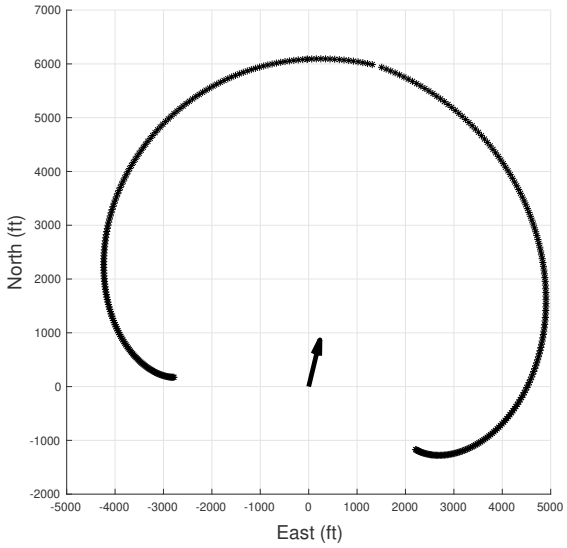


Fig. 6 Reachable Footprint with Non-Zero Wind.

C. Effects of Non-Flat Terrain

In instances where the terrain in the vicinity of the aircraft is not approximately flat, the closed-form solutions for the reachable point on the ground given by Eqs. (1)-(5) cannot be used directly. Instead, they can be spatially marched forward in time as follows. First, the total turn time t_1 can be computed and divided into smaller time intervals. The aircraft position at each time instant in the turn can be computed by solving Eqs. (1) and (2) at sequential points, swapping the initial position (x_0, y_0) and final position (x_1, y_1) as well as the initial heading ψ_0 and final heading ψ_f at each sequential point. Each propagated point in the turn can be checked for ground collision and, if it is detected, the exact point of collision can be computed through interpolation with the final two propagated points. Following the turn segment, the straight-line segment can be propagated in an analogous way. As mentioned previously, this ray-tracing process lends itself to GPU parallelization because ray tracing can occur for each candidate final heading (ψ_f) simultaneously, and because GPUs have special interpolation hardware that allows terrain checking to be performed extremely rapidly.

An example reachable footprint in complex mountainous terrain was computed using the above ray-tracing technique for a vehicle with initial location $(x_0, y_0) = (0, 0)$, altitude of $z_0 = 2100$ ft, heading of $psi_0 = 360$ deg, and zero winds. The resulting reachable footprint is shown in Fig. 7. It is evident that the footprint contours the terrain and correctly shows that the vehicle can glide farther if it turns to fly down the valley. While this is an extreme example of the effects of complex terrain, it illustrates the significant effects that terrain can have on the geometry and extent of the computed footprint.

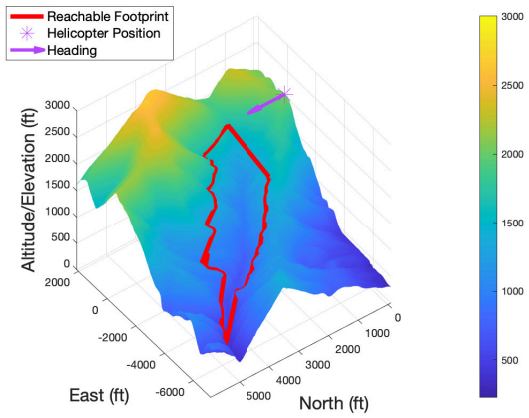


Fig. 7 Reachable Footprint Over Non-Flat Terrain.

IV. Piloted Studies

A small set of preliminary piloted studies were performed to qualitatively evaluate the utility of the reachability cue in autorotation. Resource limitations placed significant restrictions on the scope and extent of the piloted simulation trials, and thus this investigation does not constitute a complete and rigorous human factors study. Instead, the goal of these piloted trials was to solicit pilot feedback on the cueing method and to illustrate its real-time implementation as part of an avionics system. The reachability algorithm was implemented in a simulated Head Up Display at the University of Liverpool's HELIFLIGHT-R simulator [25]. This full-motion simulator is equipped with a 12 ft diameter visual dome and uses three high-resolution projectors providing a horizontal field of view of 220 deg and vertical field of view of 70 deg [26]. The simulator is driven by a FLIGHTLAB 6-degree-of-freedom flight dynamic model, and the FLIGHTLAB generic utility helicopter model is used in these studies. To visualize the reachability footprint in autorotation, markers are placed on the ground (using the HUD) at 10 deg intervals around the helicopter's current position and updated at 1 Hz as the helicopter descends. A visualization of these markers (from a perspective outside the cockpit) is provided in Fig. 8, although during simulation trials the markers were visible to the pilot through the HUD. Note that although the technology to implement this type of HUD does not presently exist for most helicopters, such a display could be implemented using a monocular cueing device such as that used in [27]. Additionally, Head Down Displays have been implemented in fixed wing aircraft for similar applications [19–21].

A series of simulated flight trials was performed at the University of Liverpool with an experienced helicopter test pilot. In each trial, autorotation was initiated from an altitude of 2,000 ft over flat terrain in good visual conditions. The aircraft was placed over an airport surrounded by suburban homes, roads, and a river. This type of ground environment provided the pilot with several options for suitable landing sites. The pilot was instructed to rapidly find a landing site near the edge of the predicted reachable footprint, and maneuver to perform a successful landing at the selected site. The reachability footprint markers were generated using the parameters in Section IIIB, and were continuously updated



Fig. 8 Screenshot of Reachable Footprint Cue Implemented at University of Liverpool.

as the maneuver progressed.

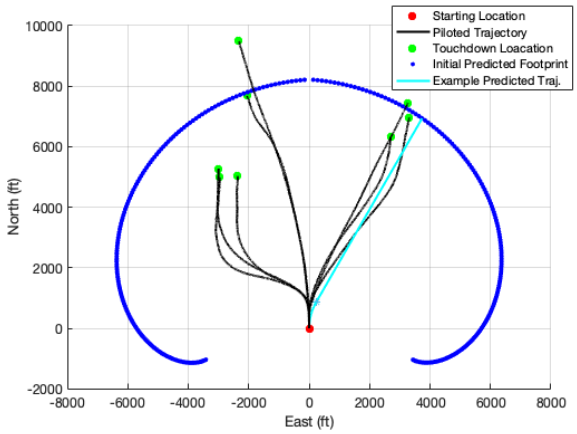


Fig. 9 Initial Reachability Footprint and Autorotation Trajectories for Piloted Simulation Trials.

Figure 9 shows the ground track of the aircraft for each of the eight trials, the landing locations (shown in green), and an example path used to compute one of the reachability markers (shown in light blue). The figure also shows the initial predicted reachable footprint in blue, although it is important to keep in mind that the footprint visible to the pilot evolves as the aircraft descends. Five of the landing points are extremely close to the initial predicted reachable footprint – note that all of these trajectories consist of an initial turn to the desired landing site, followed by an approximately straight-line path. This mirrors the trajectory used by the algorithm. Three other trajectories land well short of the initial predicted footprint – this is because two turns are performed which results in more altitude loss. Given these two turns, the trajectories should not be viewed as maximum-range trajectories and thus would not be expected to reach the bounds of the initial footprint. One landing is clearly beyond the reachable distance predicted by the footprint. This is because the pilot was able to achieve a more optimal glide condition than that used by the prediction algorithm, and also because the prediction algorithm does not include the effects of flare. However, since the footprint is, by design, a conservative prediction, landings that occur beyond the footprint are considered acceptable if they result from more

optimized descents. Subjective pilot feedback solicited after the trials indicated that the reachability cues are useful in rapidly selecting a landing site, although visualization of the cues needs to be improved. Overall, these preliminary results indicate that the proposed reachability cueing system is a promising pilot aid for rapid landing site selection, and more rigorous human factors studies are warranted.

V. Conclusion

An algorithm to predict glide distance in helicopter autorotation is presented and implemented in a basic visual display for pilot cueing. The algorithm is formulated using a simple kinematic approach amenable to rapid computation in which the aircraft turns to a desired final heading and then travels in a straight-line path until reaching the ground. The algorithm is designed to facilitate rapid selection of a landing site by a pilot by presenting a clear (conservative) upper-bound on the glide distance of the aircraft in every direction. Simulation results for the UH-60 illustrate the effects of altitude, wind, and non-flat terrain on the shape and extent of the footprint, and guidance is presented for selection of conservative algorithm parameters using simulation. A limited set of piloted flight trials highlight the effectiveness of the algorithm in predicting the reachable landing footprint and provide anecdotal evidence of the utility of the reachability cue for rapid landing site selection during emergency autorotations.

Funding Sources

This research/investigation was sponsored by the Army Research Laboratory and was accomplished under Cooperative Agreement Number W911NF-16-2-0027 and the U.S. Army/Navy/NASA Vertical Lift Research Center of Excellence with Mahendra Bhagwat serving as the Program Manager and Technical Agent, grant number W911W6-11-2- 0010, W911W6-17-2-0002 and W911NF-16-2-0027. The views and conclusions contained in this document are those of the authors and should not be interpreted as representing the official policies, either expressed or implied, of the Army Research Laboratory or the U.S. Government. The U.S. Government is authorized to reproduce and distribute reprints for Government purposes notwithstanding any copyright notation herein.

References

[1] Bachelder, E. N., and Aponso, B. L., "Using Optimal Control for Rotorcraft AutorotationTraining," *Proceedings of the 59th Annual Forum of the American Helicopter Society*, AHS, Phoenix, AZ, May 6-8, 2003.

[2] Aponso, B. L., Lee, D., and Bachelder, E. N., "Evaluation of a Rotorcraft Autorotation Training Display on a Commercial Flight Training Device," *Journal of the American Helicopter Society*, Vol. 52, No. 2, 2007, pp. 123–133. https://doi.org/10.4050/JAHS.52.123.

[3] Rogers, J., Repola, L., Jump, M., Cameron, N., and Fell, T., "Handling Qualities Assessment of a Pilot Cueing System for

Autorotation Maneuvers," *Proceedings of the 73rd Annual Forum of the American Helicopter Society*, AHS, Ft. Worth, TX, May 9-11, 2017.

[4] Rogers, J., Eberle, B., Jump, M., and Cameron, N., "Time-to-Contact-Based Control Laws for Flare Trajectory Generation and Landing Point Tracking in Autorotation," *Proceedings of the 74th Annual Forum of the American Helicopter Society*, AHS, Phoenix, AZ, 2018.

[5] Eberle, B., and Rogers, J., "Real-Time Trajectory Generation and Reachability Determination in Autorotative Flare," *Journal of the American Helicopter Society*, Vol. 65, No. 2, 2020, pp. 1–17. https://doi.org/10.4050/JAHS.65.032008.

[6] Alam, M., Jump, M., Eberle, B., and Rogers, J., "Flight Simulation Assessment of Autorotation Algorithms and Cues," *Proceedings of the 76th Annual Forum of the Vertical Flight Society*, VFS, Online, 2020.

[7] Keller, J. D., McKillip, R., Horn, J. F., and Yomchinda, T., "Active Flight Control and Appliqué Inceptor Concepts for Autorotation Performance Enhancement," *Proceedings of the 67th Annual Forum of the American Helicopter Society*, AHS, Virginia Beach, VA, May 3-5, 2011.

[8] Binet, L., Taghizad, A., Abildgaard, M., and Von Grunhagen, W., "VRS Avoidance as active function on side-sticks," *Proceedings of the 65th Annual Forum of the American Helicopter Society*, AHS, Grapevine, TX, May 27-29, 2009.

[9] Rakotomamonjy, T., Binet, L., and Müllhäuser, M., "Onera-DLR joint research on tactile cueing for reactive obstacle avoidance dedicated to low speed helicopter maneuvers," *Proceedings of the 42nd European Rotorcraft Forum*, AHS, Lille, France, Sept 5-8, 2016.

[10] Abbeel, P., Coates, A., Hunter, T., and NG, A., "Autonomous Autorotation of an RC Helicopter," *Experimental Robotics*, Vol. 54, 2009, pp. 385–394. https://doi.org/10.1007/978-3-642-00196-3_45.

[11] Sunberg, Z., Miller, N., and Rogers, J., "A Real Time Expert Control System for Helicopter Autorotation," *Journal of the American Helicopter Society*, Vol. 60, No. 2, 2015, pp. 1–15. https://doi.org/DOI:10.4050/JAHS.60.022008.

[12] Grande, N., Tierney, S., Horn, J., and Langelaan, J., "Safe Autorotation Through Wind Shear Via Backward Reachable Sets," *Journal of the American Helicopter Society*, Vol. 61, No. 2, 2016, pp. 1–11. https://doi.org/10.4050/JAHS.61.022006.

[13] Eberle, B., and Rogers, J., "Real-Time Nonlinear Model Predictive Control of a Helicopter in Autorotation," *Proceedings of the 76th Annual Forum of the Vertical Flight Society*, VFS, Online, 2020.

[14] Yomchinda, T., Horn, J., and Langelaan, J., "Flight Path Planning for Descent-phase Helicopter Autorotation," *AIAA Guidance, Navigation and Control Conference*, AIAA, Portland, OR, Aug 8-11, 2011.

[15] Coombes, M., Chen, W.-H., and Render, P., "Reachability Analysis of Landing Sites for Forced Landing of a UAS," *Journal of Intelligent Robotic Systems*, Vol. 73, 2014, pp. 635–653. https://doi.org/DOI10.1007/s10846-013-9920-9.

[16] Coombes, M., Chen, W.-H., and Render, P., "Landing Site Reachability in a Forced Landing of Unmanned Aircraft in Wind," *Journal of Aircraft*, Vol. 54, 2017, pp. 1415–1427. https://doi.org/DOI:10.2514/1.C033856.

[17] Borst, C., Sjer, F., Mulder, M., van Paassen, M. M., and Mulder, J., "Ecological Approach to Support Pilot Terrain Awareness After Total Engine Failure," *Journal of Aircraft*, Vol. 45, No. 1, 2008, pp. 159–171. https://doi.org/DOI:10.2514/1.30214.

[18] Frantis, P., "Emergency and Precautionary Landing Assistant," *IEEE/AIAA 30th Digital Avionics Systems Conference*, Institute of Electrical and Electronics Engineers, Seattle, WA, Oct. 16-20, 2011.

[19] Price, R. A., "Glide Range Depiction for Electronic Flight Instrument Displays," , U.S. Patent 6 573 841, Jun. 3, 2003.

[20] Kushwaha, D. K., "Navigating and Guiding an Aircraft to a Reachable Airport During Complete Engine Failure," , U.S. Patent 10 134 292, Nov. 20, 2018.

[21] Ogden, C. D., and Palmer, R. C., "Visualization of Glide Distance for Increased Situational Awareness," , U.S. Patent 10 242 582, Mar. 26, 2019.

[22] Osterman, A., Benedicic, L., and Ritosa, P., "An IO-efficient parallel implementation of an R2 viewshed algorithm for large terraim maps on a CUDA GPU," *International Journal of Geographical Information Science*, Vol. 28, No. 11, 2014, pp. 2304–2327. https://doi.org/10.1080/13658816.2014.918319.

[23] Dick, C., Krüger, J., and Westermann, R., "GPU Ray-Casting for Scalable Terrain Rendering," *Eurographics*, 2009.

[24] Fowler, L., Rogers, J., sarkar, S., and Iyyer, N., "A Virtual Pilot Algorithm for Synthetic HUMS Data Generation," *Journal of the American Helicopter Society*, Vol. 62, 2017, pp. 1–14. https://doi.org/10.4050/JAHS.62.042006.

[25] White, M., Perfect, P., Padfield, G., Gubbels, A., and Berryman, A., "Acceptance testing and commissioning of a flight simulator for rotorcraft simulation fidelity research," *Proceedings of the Institution of Mechanical Engineers, Part G: Journal of Aerospace Engineering*, Vol. 227, No. 4, 2012, pp. 663–686. https://doi.org/10.1177/0954410012439816.

[26] Memon, W. A., Owen, I., and White, M., "Motion Fidelity Requirements for Helicopter-Ship Operations in Maritime Rotorcraft Flight Simulators," *Journal of Aircraft*, Vol. 56, No. 6, 2019, pp. 1–21. https://doi.org/10.2514/1.C035521.

[27] Taylor, T., "Rotorcraft Visual Situational Awareness (VSA): Solving the Pilotage Problem for Landing in Degraded Visual Environments," *SPIE 7328, Enhanced and Synthetic Vision*, Society of Photo-Optical Instrumentation Engineers, Orlando, FL, May 6 2009.



https://dspace.org/

Rapid method for computing reachable landing distances in helicopter autorotative descent

Eberle, Brian F.; Rogers, Jonathan; Alam, Mushfiqul; Jump, Michael

2022-05-25
AIAA
https://doi.org/10.2514/1.I011035
Eberle BF, Rogers JD, Alam M, Jump M. (2022) Rapid method for computing reachable landing distances in helicopter autorotative descent. Journal of Aerospace Information Systems, Volume 19, Number 7, July 2022, pp. 504-510

Downloaded from a DSpace repository. https://dspace.org/